Check for updates

Polaritons in Non-Fullerene Acceptors for High Responsivity Angle-Independent Organic Narrowband Infrared Photodiodes

Ahmed Gaber Abdelmagid, Zhuoran Qiao, Boudewijn Coenegracht, Gaon Yu, Hassan A. Qureshi, Thomas D. Anthopoulos, Nicola Gasparini, and Konstantinos S. Daskalakis**

Narrowband infrared organic photodetectors are in great demand for sensing, imaging, and spectroscopy applications, in particular for handheld and wearable devices, in which miniaturization is essential. However, most existing strategies for narrowband detection depend on spectral filtering either through saturable absorption, which requires active layers exceeding 500 nm, restricting the choice of materials for producing high-quality films, or cavity effects, which inherently introduce strong angular dispersion. Microcavity exciton-polariton (polariton) modes, which emerge from strong exciton-photon coupling, have recently been explored as an angular dispersion suppression strategy for organic optoelectronics. In this work, the first narrowband infrared polariton organic photodiode that combines angle-independent response with a record-high responsivity of 0.24 A W^{-1} at 965 nm and –2 V is presented. This device, featuring a 100-nm-thin active layer comprising a non-fullerene acceptor, exhibits a detection mode with a full-width at half-maximum of less than 30 nm and a marginal angular dispersion of under 15 nm across ±45°. This study highlights the potential of polaritons as an innovative platform for developing next-generation optoelectronic devices that achieve simultaneous enhancements in optical and electronic performance.

1. Main

Photodiodes are essential solid-state devices that convert light into electrical signals, playing a pivotal role in photonics and materials research.[1–3] Their applications span from basic light detection to sophisticated multicolor imaging in telecommunications, machine vision, and microscopy, where color selectivity is a critical performance factor. Organic photodiodes (OPDs) have gained significant attention for their fabrication simplicity and mechanical flexibility.[4,5] However, narrowband detection is challenging.[6–9] Two primary strategies are employed to address this challenge. The first involves manipulating internal quantum efficiency by controlling charge collection efficiency (CCN) and exciton dissociation efficiency (EDN). This approach utilizes a thick bulk heterojunction (BHJ) layer to enable selective wavelength response by promoting

---

A. G. Abdelmagid, B. Coenegracht[+], G. Yu[++], H. A. Qureshi,
K. S. Daskalakis
Department of Mechanical and Materials Engineering
University of Turku
FI-20014 Turku, Finland
E-mail: ahmed.abdelmagid@utu.fi; konstantinos.daskalakis@utu.fi

The ORCID identification number(s) for the author(s) of this article can be found under https://doi.org/10.1002/adom.202501727

[+]Present address: Molecular Materials and Nanosystems and Institute for Complex Molecular Systems, Eindhoven University of Technology, Eindhoven, Netherlands

[++]Present address: Graduate Institute of Ferrous and Eco Materials Technology, Pohang University of Science and Technology, Pohang 37673, Republic of Korea

© 2025 The Author(s). Advanced Optical Materials published by Wiley-VCH GmbH. This is an open access article under the terms of the Creative Commons Attribution License, which permits use, distribution and reproduction in any medium, provided the original work is properly cited.

DOI: 10.1002/adom.202501727

Z. Qiao, N. Gasparini
Department of Chemistry and Centre for Processable Electronics
Imperial College London, White City Campus
82 Wood Lane, London W12 0BZ, UK

T. D. Anthopoulos
Henry Royce Institute and Photon Science Institute, Department of Electrical and Electronic Engineering
The University of Manchester
Oxford Road, Manchester M13 9PL, UK

T. D. Anthopoulos
King Abdullah University of Science and Technology (KAUST)
KAUST Solar Centre (KSC)
Thuwal 23955-6900, Saudi Arabia

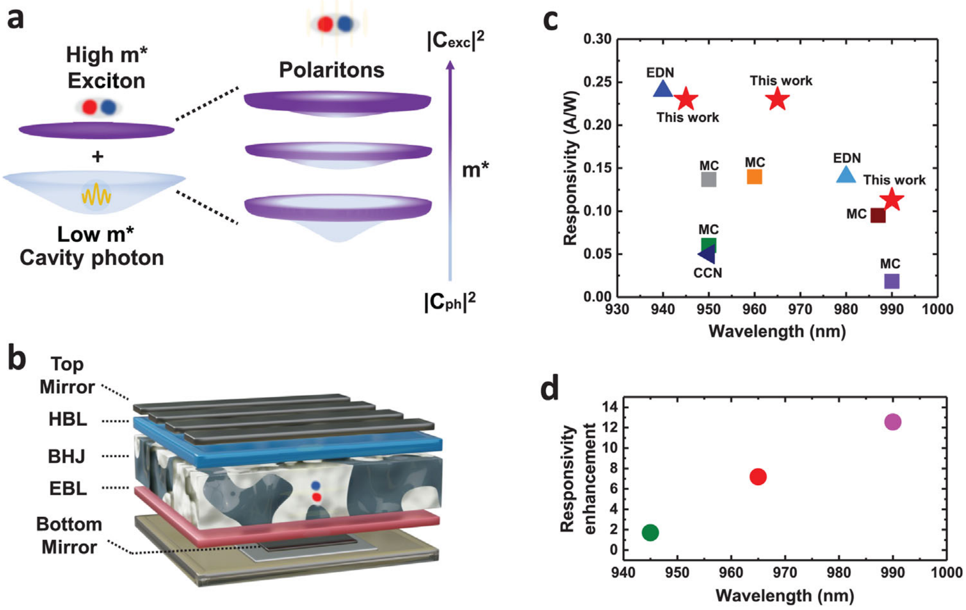

Figure 1. a) Schematic illustration of the impact of strong exciton-photon coupling on the effective mass and polariton dispersion. As the exciton content rises, the effective mass increases, resulting in a flatter dispersion. Two-level conceptual model shown for clarity. b) Simplified scheme of the polariton OPD with a sketch of the interaction between the cavity resonance and the exciton. c) Comparison of the responsivities of narrowband OPDs at 0 V with peak wavelengths between 940 and 990 nm (Table 1, Supporting Information). d) The responsivity enhancement of the polariton OPDs with device resonance at 945 nm (olive), 965 nm (red), 990 nm (magenta). The developed polaritonic OPD constructed from layers of (glass/ITO (Electrode)/Ag 25 nm (Bottom Mirror)/MoO_3 10 nm (EBL)/PTB7-Th:IEICO-4F (BHJ)/C_{60}:LiF 25 nm (HBL)/Ag 150 nm (Top Mirror/Electrode)), with light entering from the ITO side.

recombination at shorter wavelengths.[10–13] The second strategy incorporates a microcavity (MC), which enhances absorption at specific wavelengths determined by the cavity's refractive index (n) and thickness (L).[14–21] These approaches have trade-offs: in the CCN approach, it is feasible with only a limited selection of organic semiconductor materials and often introduces challenges in processing, while microcavities inherit the OPD a strong angular dispersion.[15,20,21] However, compared to CCN, microcavities offer several distinct advantages making them a superior approach.[8] They can enhance spectral selectivity, extend responsivity, and achieve these enhancements within optimized OPD architectures that already exhibit excellent optoelectronic performance.[7–9] Furthermore, their versatility allows for seamless integration into existing device designs.[22]

An additional advantage of optical microcavities is their ability to facilitate strong coupling between excitons and cavity photons, forming hybrid states known as polaritons that inherit properties from light and matter.[23,24] In OPDs, highly localized Frenkel excitons with a large effective mass are common. Reports indicate that under strong coupling, Frenkel excitons exhibit delocalization and low effective mass of cavity photons, leading to enhanced exciton diffusion,[25–30] and suppression of exciton-exciton annihilation processes.[31–33] These effects can enhance the electrical properties, stability, and overall functionality of organic optoelectronic devices. Moreover, polaritons can be viewed as cavity modes dressed with "heavy" excitons, which have a mass m_{exc}. This coupling results in an angular dispersion that is significantly flatter than that of bare cavity photons with mass m_{ph}. The reduced curvature reflects an increase in the effective mass of the polariton, m_{pol}, which depends on the exciton-photon mixing ratio, as described by:

$$\frac{1}{m_{pol}} = \frac{|C_{ph}|^2}{m_{ph}} + \frac{|C_{exc}|^2}{m_{exc}} \tag{1}$$

Here, $|C_{ph}|^2$ and $|C_{exc}|^2$ are the Hopfield coefficients that denote the photon and exciton fractions of the polariton mode, respectively, with $|C_{ph}|^2 + |C_{exc}|^2 = 1$. By increasing the exciton content $|C_{exc}|^2$, the effective mass m_{pol} increases, leading to a suppression of the polariton dispersion (**Figure** 1a).[34] Increasing the exciton content in the polariton mode can be achieved by either increasing the cavity-exciton detuning or the coupling strength of the system.[23,34] This approach has recently been used to suppress angular dispersion in infrared polariton microcavities,[35] carbon nanotube photodiodes,[36] optical filters,[37] and organic light-emitting diodes.[38,39] However, a significant challenge remains: demonstrating polaritonic optoelectronic devices that not only outperform their non-polaritonic counterparts but also exceed the performance benchmarks typically reported in the field. Achieving such breakthrough results is crucial for realizing the full potential of polariton-based technologies in practical applications.

Here, we demonstrate, for the first time, a narrowband polariton OPD (Figure 1b) that utilizes the polariton photonic gains while reaching a high responsivity in the infrared region from ≈ 945–990 nm (Figure 1c). Note, here we consider as narrowband a detection bandwidth with a full-width at half-maximum (FWHM) of less than 100 nm,[9] and in our reported devices

© 2025 The Author(s). Advanced Optical Materials published by Wiley-VCH GmbH

21951071, 0, Downloaded from https://advanced.onlinelibrary.wiley.com/doi/10.1002/adom.202501727 by Duodecim Medical Publications Ltd, Wiley Online Library on [29/08/2025]. See the Terms and Conditions (https://onlinelibrary.wiley.com/terms-and-conditions) on Wiley Online Library for rules of use; OA articles are governed by the applicable Creative Commons License

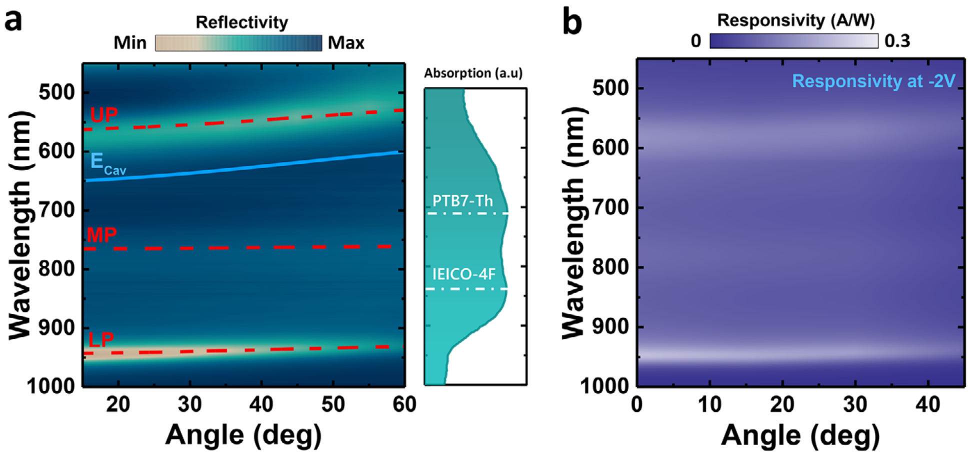

Figure 2. a) Polariton characteristics of the polariton OPD. Angle-resolved reflectivity of polariton OPD with device resonance of 945 nm from 15° to 60°. The solid blue line is the cavity energy dispersion, and the dashed red lines are fitted polariton dispersions. Besides is the absorption of the active blend and the dashed white line is the molecular exciton energies of PTB7-Th and IEICO-4F. b) Polariton characteristics under negative electrical bias. The angle-resolved responsivity of the polariton device from 0° to 45° at –2 V.

this was less than 45 nm. In particular, at 965 nm we recorded a responsivity of 0.23 A W^{-1} at 0 V, which is the highest reported to date[10,12,13,15,16,18–20] (see Figure 1c for devices operating at 945 and 990 nm). Importantly, we achieved these metrics with 100-nm active layer OPDs which are substantially thinner than prior state-of-the-art (see Table 1, Supporting Information). Interestingly, compared with the reference device (see Experimental Section), these represent a seven-fold enhancement at 965 nm (see Figure 1d; Figure S1, Supporting Information). Importantly, these polariton OPDs achieved such optical response while maintaining low angular dispersion of less than 17 nm within an observation cone of ±45° (see analysis in Section 3.2 and Figure 3).

In this work, the active medium of the polariton OPDs is a blend of PTB7-Th:IEICO-4F. We selected IEICO-4F because of its high oscillator strength,[40] and good film morphology when blended with PTB7-Th[41] - both essential for reaching strong coupling in planar microcavities.[42] IEICO-4F belongs to the class of nonfullerene acceptors (NFAs) that offer future possibilities to tune their absorption resonance down to the visible wavelength range via molecular design.[43–45] Furthermore, NFAs have been extensively exploited in organic optoelectronic devices, enabling efficient organic photovoltaics (OPVs)[46–49] and broadband OPDs[50–53] due to their high charge mobility, efficient charge transport, and chemical and thermal stability.

Figure 2a presents the angle-resolved reflectivity map of a polariton OPD with an active layer thickness of ≈92 nm (see Experimental Section). There, three distinct reflectivity dips appear, corresponding to the upper, middle, and lower polariton branches, respectively. In this study, we focus on the lower polariton mode, as its resonance falls within the investigated spectral range. Henceforth, “device resonance” refers to the lower polariton resonance. The corresponding angle-resolved reflectivity spectra are shown in Figure S2 (Supporting Information). The presence of three polariton branches indicates effective coupling between the cavity mode and the molecular excitons of PTB7-Th (710 nm) and IEICO-4F (835 nm), as highlighted by the dashed white lines. By fitting the data with a coupled harmonic oscillator (CHO) model, we determined the cavity resonance at 656 nm at an incidence angle of 0°; the cavity dispersion is shown as a solid blue line. The fitted polariton dispersions are depicted as dashed red lines. For these modes, our fitting results to a Rabi splitting of 0.57 and 0.31 eV and detuning of $\Delta = E_c - E_{IEICO-4F} = 0.41$ eV. Figure S3 (Supporting Information) illustrates the exciton and photon fractions of the lower polariton (LP) branch, revealing a significant exciton contribution from IEICO-4F, ≈60%. This high exciton content enhances the effective mass of the polariton and results in an exciton-like optical response, as seen in Figure 2a.[34] Additional analysis for polariton OPDs with device resonances at 965 and 990 nm are provided in the Supporting Information.

To verify that the device operates in the strong coupling regime under bias, we performed angle-resolved responsivity measurements for the polariton OPD operating at 945 nm at –2 V. As shown in Figure 2b, there is excellent agreement between reflectivity and responsivity measurements. While Y6 cavity optimization (Figure S5) confirmed the general applicability of our strategy to other NFAs, IEICO-4F was selected for full device fabrication based on its superior NIR performance in published OPD architectures.[50,51]

Figure 3a shows angle-resolved responsivity maps from polariton OPDs with device resonance of 945 nm (top) and 965 nm (bottom). Angle-resolved spectra are shown in Supporting Information. Our devices exhibit responsivities above 0.096 A W^{-1} within their acceptance cone of ±45°. Within this range, the responsivity peak shifts by 9 nm for the thinnest OPDs and up to 16 nm for the thickest (Figure 3b), which is substantially suppressed compared to reported narrowband conventional microcavity-enhanced OPDs.[15,20,21] This reduced angular dependency highlights the benefits of strong coupling within our devices and is directly correlated with the exciton content in the LP (see Figure S6, Supporting Information). Because angle-resolved responsivity measurements were limited to 5 nm spectral resolution, it overestimated the angle dispersion of our devices. To circumvent this, we used an in-house built angle-resolved reflectivity setup with a spectral resolution of 0.4 nm.[54]

At normal incidence, the FWHM of the responsivity peak is less than 45 nm for all devices (Figure 3c). This narrow FWHM

© 2025 The Author(s). Advanced Optical Materials published by Wiley-VCH GmbH

21951071, 0, Downloaded from https://onlinelibrary.wiley.com/doi/10.1002/adom.202501727 by Duodecim Medical Publications Ltd, Wiley Online Library on [29/08/2025]. See the Terms and Conditions (https://onlinelibrary.wiley.com/terms-and-conditions) on Wiley Online Library for rules of use; OA articles are governed by the applicable Creative Commons License

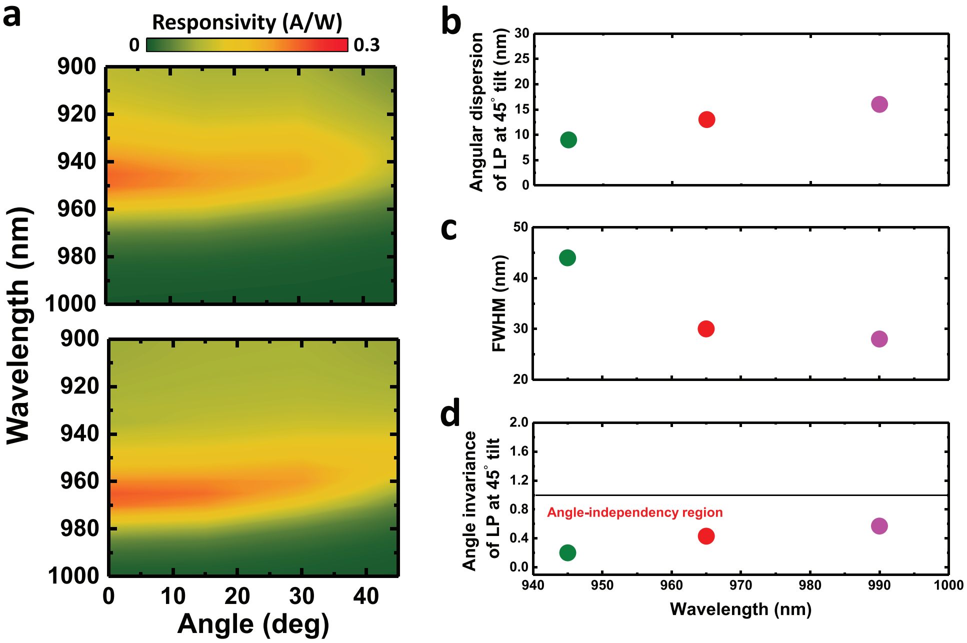

Figure 3. a) Angle-resolved responsivity maps from 0° to 45° with an interval of 15° for the polariton OPDs with device resonance of 945 nm (top) and 965 nm (bottom) b) Angular dispersion, c) FWHM, and d) Angle invariance for the polariton OPDs with device resonance of 920 nm (olive), 965 nm (red), and 990 nm (magenta).

is achieved by tuning the mode to the above-gap, low-absorption region of the active material, where reduced absorption allows for enhanced narrowband polariton effects with strong angular stability. We highlight this effect in Figure 3d where we plot the angle invariance factor, defined as angular dispersion over the FWHM, with wavelength, showing that all devices are in principle angle independent.

We explored the limitations of our device architecture by tuning the resonance to shorter wavelengths at 920 nm. This resulted in a significantly broader FWHM of more than 100 nm and a reduced responsivity compared to the reference device (Figure S7, Supporting Information). We speculate that this is because the mode in this device overlaps substantially with a high-absorption region of the active material, which dampens the resonance and reduces both the polariton-enhanced spectral narrowing and the overall device efficiency.[11,14,15]

Figure 4a shows the characteristic current-voltage measurement from polariton OPD with resonance wavelength 965 nm in dark and illuminated conditions. A dark current density of 9.29×10^{-7} A cm^{-2} at -2 V was recorded. This relatively high value is attributed to the lack of optimization of the hole and electron blocking layers, which is beyond the scope of this study. Under the illumination conditions (see Methods), we observe a photocurrent density (J_L) value of 1.04×10^{-3} A cm^{-2} at –2 V.

As previously discussed, we have achieved a maximum responsivity of 0.23 A W^{-1} at 965 nm and 0 V, which peaked at 0.24 A W^{-1} when biased at –2 V, which are the typical operating conditions of OPDs.[55] Figure 4b presents the responsivity spectra of the polariton OPD at -2 V, while Figure S8 (Supporting Information) displays the responsivity across various bias voltages. Such bias independence indicates an enhanced charge extraction and collection within the active layer under reverse bias.[56] Moreover, parasitic responsivity is less than 0.10 A W^{-1} for broadband illumination except at the UP resonance that goes to 0.12 A W^{-1}.

The specific detectivity (D^*) can be calculated using the responsivity and noise spectral density (see Experimental section). However, D^* can be overestimated when shot noise, which is derived from dark current, is considered solely as the origin of noise since other sources of noise including flicker and thermal noise, will also contribute significantly to the overall noise in the device[57]. Therefore, in this work, noise spectral density was calculated through the fast Fourier transform (FFT) of the dark current (Figure S10, Supporting Information). We calculated D^*_{measured} to be 5.93×10^9 Jones at –2 V at 965 nm.

Dynamic measurements were conducted to assess the operation speed of the polariton OPD at –2 V. The polariton OPD exhibited a rise time of 1.6 µs and a fall time of 1.1 µs under IR light illumination (Figure 4c). Additionally, the cut-off frequency, defined as the frequency at which the photocurrent response diminishes by 3 dB from its low-frequency value, was measured to be 412 kHz under 970 nm illumination (Figure 4d). These results demonstrate the potential of the polariton OPD to be applied for fast imaging applications.[6,57]

For comparison, the reference device exhibited a broadband response with spectral responsivity exceeding 0.40 A W^{-1} and an EQE of over 65% in the 760–860 nm range. However, these values declined beyond 900 nm due to the reduced absorption of IEICO-4F. The responsivity of the reference device, measured under different bias, is shown in Figure S9 (Supporting Information). In contrast, as previously demonstrated, the responsivity spectra of the polariton OPD differed significantly from those of the reference device. Despite this, all key performance metrics of the polariton OPD were comparable to those of the reference device (see Figure S11, Supporting Information), indicating that

© 2025 The Author(s). Advanced Optical Materials published by Wiley-VCH GmbH

21951071, 0, Downloaded from https://advanced.onlinelibrary.wiley.com/doi/10.1002/adom.202501727 by Duodecim Medical Publications Ltd, Wiley Online Library on [29/08/2025]. See the Terms and Conditions (https://onlinelibrary.wiley.com/terms-and-conditions) on Wiley Online Library for rules of use; OA articles are governed by the applicable Creative Commons License

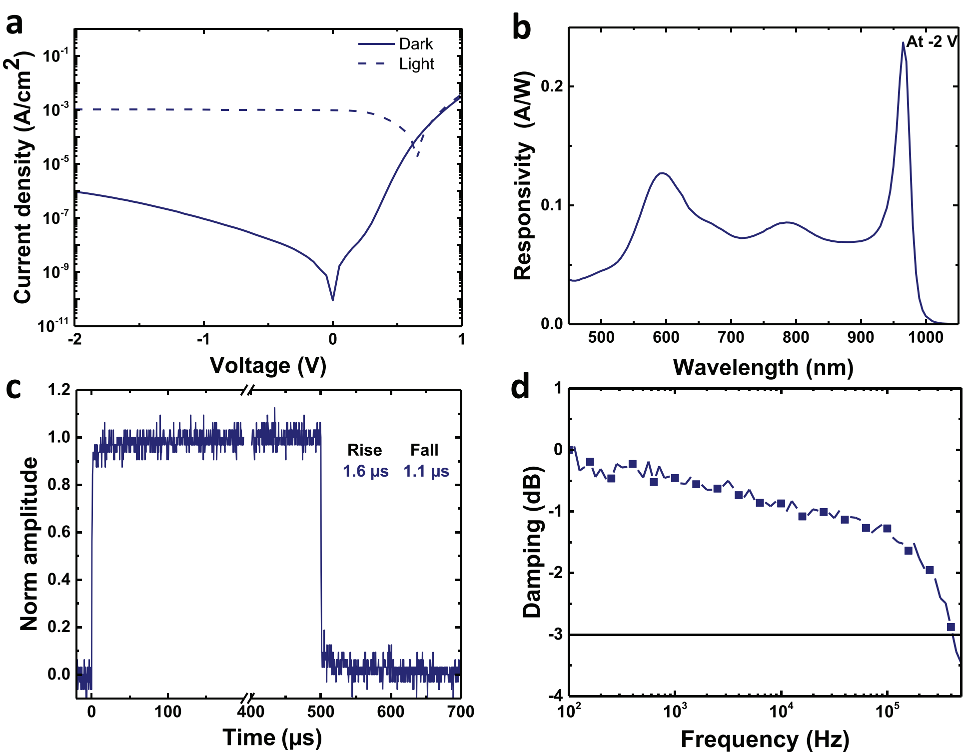

Figure 4. a) Dark and light J-V curve of the optimized device, polariton OPD with resonance wavelength at 965 nm. b) Responsivity at –2 V. c) Transient photoresponse of the polariton OPD at –2 V under 970 nm NIR light. d) Cut-off frequency of the polariton OPD at –3 dB at –2 V under 970 nm NIR light.

the integration of polaritons into the broadband device did not negatively impact its performance.

2. Conclusion and Outlook

In this work, we have demonstrated the first narrowband polariton organic photodiodes with responsivity that surpasses the performance of previously reported narrowband OPDs in the near-infrared (NIR) region. By employing a Fabry-Pérot cavity design and leveraging the strong coupling regime, we achieved narrowband detection with FWHM of less than 45 nm and responsivity values up to 0.24 A W^{-1} at 965 nm, at –2 V bias. The devices showed minimal dispersion across a wide angular acceptance cone of ±45°, showcasing the angle-independent nature of our devices.

Our work highlights the potential of integrating polaritonic enhancements in OPDs, demonstrating their ability to improve spectral selectivity and suppress angular dispersion without compromising their figures of merit. The choice of non-fullerene acceptor IEICO-4F was instrumental in achieving strong coupling in the NIR spectrum because of its high oscillator strength in this spectral range. Additionally, our findings confirm that polaritonic devices can maintain performance metrics comparable to, or even exceeding, those of conventional broadband OPDs. Moreover, NFAs provide a versatile platform for expanding the operating wavelength range, as their absorption properties can be molecularly tailored to cover both the visible and infrared regions.[43,44] This study demonstrates that OPDs represent an exceptionally promising device configuration where polaritonic effects can lead to substantial improvements in performance. Our approach lays the groundwork for the development of high-performance, angle-independent polaritonic optoelectronic devices, offering promising applications in imaging, sensing, and spectroscopy.

3. Experimental Section

Materials: PTB7-Th, IEICO-4F, and Y6 were purchased from 1-material. C_{60} was purchased from Lumtec.

Microcavity and Device Fabrication: Glass substrates prepatterned with ITO (15mm × 15mm × 0.7mm) were cleaned with water/soap (3 % Decon 90), acetone, and Isopropanol solutions to remove any residue from the surfaces. The substrates were sonicated for 10 min on each step and finally dried with a N_2 purge. A similar cleaning protocol was deployed for the silicon substrates that were used to measure the thicknesses with ellipsometry. **Thin-Film Microcavities**: IEICO-4F and Y6 were dissolved in chloroform at a concentration of 16 mg mL^{-1}, then stirred for 2 h at 80°C, followed by one hour at 60°C inside a glovebox. Thin-film microcavities were fabricated by spin-coating the NFA solution onto a 120 nm Ag layer at 2500 rpm for Y6 and 3000 rpm for IEICO-4F, each for 30 s. The films were then annealed at 100°C for 10 min in the glovebox, followed by the evaporation of a 30 nm Ag layer as the top mirror.

Device Fabrication: polariton OPDs were fabricated in the architecture of (glass/ITO/Ag 25 nm/MoO_3 10 nm/PTB7-Th:IEICO-4F/C_{60}:LiF 25 nm/Ag 150 nm). The bottom silver mirror and MoO_3 were deposited using an Angstrom evaporation system. The photoactive blend (PTB7-Th:IEICO-4F) was deposited in a glovebox. the blend was spin-coated from a 25 mg mL^{-1} solution in chlorobenzene:chloronaphthaline (96:4 v/v)at different rpm with the same annealing protocol used for the neat NFA films. The active layer thicknesses were varied by varying the rpm. On top of the photoactive layer, a C_{60}:LiF (1:4) layer was then deposited via co-evaporation.

© 2025 The Author(s). Advanced Optical Materials published by Wiley-VCH GmbH

21951071, 0, Downloaded from https://advanced.onlinelibrary.wiley.com/doi/10.1002/adom.202501727 by Duodecim Medical Publications Ltd, Wiley Online Library on [29/08/2025]. See the Terms and Conditions (https://onlinelibrary.wiley.com/terms-and-conditions) on Wiley Online Library for rules of use; OA articles are governed by the applicable Creative Commons License

Finally, 150 nm-thick Ag was deposited as the top electrode by evaporation through a shadow mask giving photodiodes with pixel areas of 0.08 cm^2. The reference device was identical to the polariton device but did not include the thin Ag layer. All devices were encapsulated using a glass cover-slip and a UV-curable epoxy (Ossila Ltd) prior to characterization.

Optical Characterization: The thicknesses of the thin films were acquired using a J.A Wollam VASE ellipsometer. We utilized an Xe lamp with a spectral range of 250–2500 nm to obtain the spectra, the data was analyzed by fitting a Cauchy model in the transparent region of the film. The dispersion of the microcavities and devices was obtained with the VASE ellipsometer and a custom-built angle-resolved imaging setup. The setup uses a collimated light from a halogen lamp illuminating the sample through a 0.75 NA microscope objective. The reflected light is then collected with the same objective and the back focal plane image is then focused into the slit of the spectrometer that is coupled to a 2D CCD camera (1340 × 400 pixels). The reflectivity dispersion was then resolved in wavelength vs angle. The couple harmonic oscillator model was used to fit the polariton modes and extract the Rabi splitting energy, cavity resonance, and Hopfield coefficients.

Electrical Characterization: *J–V* measurements were conducted using a Keithley 4200 Source-Measure unit (scan rate 50 mV s^{-1}). An Oriel Instruments Solar Simulator with a Xenon lamp and calibrated to a silicon reference cell was used to provide AM1.5G irradiance. External quantum efficiency (EQE) was measured using an integrated system from Quantum Design PV300 with a modulation frequency of 90 Hz. Responsivity was further calculated using equation

$$R = \mathrm{EQE} \cdot \frac{q\lambda}{hc} \tag{2}$$

Where q is elementary charge, λ is the wavelength of the light, h is Planck constant, and c is the speed of light. All the devices were tested in ambient air. Specific detectivity was calculated using equation

$$D^* = \frac{R\sqrt{A\Delta f}}{i_n} \tag{3}$$

Where R is responsivity, A denoted the device photoactive area, Δf is the detection bandwidth and i_n is the noise spectral density. Here, to accurately evaluate specific detectivity, i_n was calculated by the fast Fourier transform of the dark current obtained from a digital oscilloscope (Siglent, SDS6054A) with combination of a FEMTO-100 preamplifier under –2 V. The specific detectivity value can be overestimated by considering solely the contribution of dark current (i_{shot}) to the noise using equation

$$i_{shot} = \sqrt{2qI_d} \tag{4}$$

Where I_d refers to the dark current. Dynamic measurements were performed using the digital oscilloscope (Siglent, SDS6054A). The OPDs were illuminated with a 970 nm LED driven by a function generator (ThorLabs DC2200). For determination of the rise and fall time, which is defined as the time interval in which the output photocurrent increases from 10% to 90% and diminishes from 90% down to 10% of the peak photocurrent, a 1 kHz square wave pulse was applied to the LED using the function generator. For determination of the cut-off frequency, sinusoidal functions with varying frequencies between 100 Hz and 1 MHz were used to drive the LED from the function generator. All the devices were tested in ambient air.

Supporting Information

Supporting Information is available from the Wiley Online Library or from the author.

Acknowledgements

This project has received funding from the European Research Council (ERC) under the European Union's Horizon 2020 research and innovation programme (grant agreement No. [948260]) and by the European Innovation Council through the project SCOLED (Grant Agreement Number 101098813). Views and opinions expressed are however those of the author(s) only and do not necessarily reflect those of the European Union or the European Innovation Council and SMEs Executive Agency (EISMEA). Neither the European Union nor the granting authority can be held responsible for them. ZQ and NG thank the King Abdullah University of Science and Technology (KAUST) Office of Sponsored Research (OSR) under Award No. OSR-2020-CRG8-4095 and ORFS-2023-OFP-5544.

Author Contributions

AGA, TDA, and KSD initiated the project. AGA designed the project, fabricated the devices, performed the majority of experiments, and analyzed the data. ZQ together with AGA performed the optoelectronic measurements, supervised by NG. HAQ performed the high-resolution reflectivity measurements. BC and GY contributed to the sample fabrication and characterization. AGA and KSD wrote the manuscript. KSD supervised the project. All authors contributed to the draft, discussion, and analysis of the data.

Conflict of Interest

The authors declare no conflict of interest.

Data Availability Statement

The data that support the findings of this study are available from the corresponding author upon reasonable request.

Keywords

microcavities, narrowband infrared organic photodiodes, non-fullerene acceptors, polaritons

Received: May 29, 2025
Revised: July 16, 2025
Published online:

---

[1] Z. Lan, M.-H. Lee, F. Zhu, *Adv. Intell. Syst.* **2022**, *4*, 2100167.
[2] X. Zhang, J. Jiang, B. Feng, H. Song, L. Shen, *J. Mater. Chem. C* **2023**, *11*, 12453.
[3] T. Li, G. Hu, H. Wu, L. Ding, J. Zhang, M. Sun, Y. Li, Z. Liu, Y. Shao, Y. Fang, Y. Qiao, L. Shen, Y. Lin, *Nat. Water* **2024**, *2*, 577.
[4] Y. Wang, T. Zhang, D. Samigullina, L. C. Winkler, F. Dollinger, J. Kublitski, X. Jia, R. Ji, S. Reineke, D. Spoltore, K. Leo, J. Benduhn, *Adv. Funct. Mater.* **2024**, *34*, 2313689.
[5] Z. Wang, S. Cheng, K. Fukuda, W. Hu, X. Xu, T. Someya, *Wearable Electron.* **2024**.
[6] R. D. Jansen-van Vuuren, A. Armin, A. K. Pandey, P. L. Burn, P. Meredith, *Adv. Mater.* **2016**, *28*, 4766.
[7] J. Vanderspikken, W. Maes, K. Vandewal, *Adv. Funct. Mater.* **2021**, *31*, 2104060.
[8] Y. Wang, J. Kublitski, S. Xing, F. Dollinger, D. Spoltore, J. Benduhn, K. Leo, *Mater. Horiz.* **2022**, *9*, 220.
[9] X. Zhao, J. Wang, M. Liu, X. Ma, F. Zhang, *Adv. Opt. Mater.* **2024**, *12*, 2401087.
[10] A. Armin, R. D. Jansen-van Vuuren, N. Kopidakis, P. L. Burn, P. Meredith, *Nat. Commun.* **2015**, *6*, 6343.

© 2025 The Author(s). Advanced Optical Materials published by Wiley-VCH GmbH

21951071, 0, Downloaded from https://advanced.onlinelibrary.wiley.com/doi/10.1002/adom.202501727 by Duodecim Medical Publications Ltd, Wiley Online Library on [29/08/2025]. See the Terms and Conditions (https://onlinelibrary.wiley.com/terms-and-conditions) on Wiley Online Library for rules of use; OA articles are governed by the applicable Creative Commons License

[11] Q. Lin, A. Armin, P. L. Burn, P. Meredith, *Nat. Photonics* **2015**, *9*, 687.
[12] B. Xie, R. Xie, K. Zhang, Q. Yin, Z. Hu, G. Yu, F. Huang, Y. Cao, *Nat. Commun.* **2020**, *11*, 2871.
[13] Q. Liu, S. Zeiske, X. Jiang, D. Desta, S. Mertens, S. Gielen, R. Shanivarasanthe, H.-G. Boyen, A. Armin, K. Vandewal, *Nat. Commun.* **2022**, *13*, 5194.
[14] J. M. Lupton, R. Koeppe, J. G. Müller, J. Feldmann, U. Scherf, U. Lemmer, *Adv. Mater.* **2003**, *15*, 1471.
[15] B. Siegmund, A. Mischok, J. Benduhn, O. Zeika, S. Ullbrich, F. Nehm, M. Böhm, D. Spoltore, H. Fröb, C. Körner, K. Leo, K. Vandewal, *Nat. Commun.* **2017**, *8*, 15421.
[16] Z. Tang, Z. Ma, A. Sánchez-Díaz, S. Ullbrich, Y. Liu, B. Siegmund, A. Mischok, K. Leo, M. Campoy-Quiles, W. Li, K. Vandewal, *Adv. Mater.* **2017**, *29*, 1702184.
[17] J. Wang, S. Ullbrich, J.-L. Hou, D. Spoltore, Q. Wang, Z. Ma, Z. Tang, K. Vandewal, *ACS Photonics* **2019**, *6*, 1393.
[18] J. Vanderspikken, Q. Liu, Z. Liu, T. Vandermeeren, T. Cardeynaels, S. Gielen, B. Van Mele, N. Van den Brande, B. Champagne, K. Vandewal, W. Maes, *Adv. Funct. Mater.* **2022**, *32*, 2108146.
[19] S. Xing, V. C. Nikolis, J. Kublitski, E. Guo, X. Jia, Y. Wang, D. Spoltore, K. Vandewal, H. Kleemann, J. Benduhn, K. Leo, *Adv. Mater.* **2021**, *33*, 2102967.
[20] Y. Wang, B. Siegmund, Z. Tang, Z. Ma, J. Kublitski, S. Xing, V. C. Nikolis, S. Ullbrich, Y. Li, J. Benduhn, D. Spoltore, K. Vandewal, *Adv. Opt. Mater.* **2021**, *9*, 2001784.
[21] J. Yang, J. Huang, R. Li, H. Li, B. Sun, Q. Lin, M. Wang, Z. Ma, K. Vandewal, Z. Tang, *Chem. Mater.* **2021**, *33*, 5147.
[22] E. Palo, K. S. Daskalakis, *Adv. Mater. Interfaces* **2023**, *10*, 2202206.
[23] A. Frisk Kockum, A. Miranowicz, S. De Liberato, S. Savasta, F. Nori, *Nat. Rev. Phys.* **2019**, *1*, 19.
[24] F. J. Garcia-Vidal, C. Ciuti, T. W. Ebbesen, *Science* **2021**, *373*, eabd0336.
[25] D. M. Coles, N. Somaschi, P. Michetti, C. Clark, P. G. Lagoudakis, P. G. Savvidis, D. G. Lidzey, *Nat. Mater.* **2014**, *13*, 712.
[26] B. Xiang, R. F. Ribeiro, M. Du, L. Chen, Z. Yang, J. Wang, J. Yuen-Zhou, W. Xiong, *Science* **2020**, *368*, 665.
[27] M. Wang, M. Hertzog, K. Börjesson, *Nat. Commun.* **2021**, *12*, 1874.
[28] M. Balasubrahmaniyam, A. Simkhovich, A. Golombek, G. Sandik, G. Ankonina, T. Schwartz, *Nat. Mater.* **2023**, *22*, 338.
[29] I. Sokolovskii, R. H. Tichauer, D. Morozov, J. Feist, G. Groenhof, *Nat. Commun.* **2023**, *14*, 6613.
[30] G. Sandik, J. Feist, F. J. García-Vidal, T. Schwartz, *Nat. Mater.* **2024**, *24*, 344.
[31] H. Zhao, C. E. Arneson, D. Fan, S. R. Forrest, *Nature* **2024**, *626*, 300.
[32] C. E. Arneson, H. Zhao, S. R. Forrest, *Adv. Funct. Mater.* **2024**, *34*, 2410741.
[33] H. A. Qureshi, M. A. Papachatzakis, A. G. Abdelmagid, M. Salomäki, E. Mäkilä, O. Siltanen, K. S. Daskalakis, *Adv. Opt. Mater.* **2025**, *13*, 2500155.
[34] H. Deng, H. Haug, Y. Yamamoto, *Rev. Mod. Phys.* **2010**, *82*, 1489.
[35] E. Eizner, J. Brodeur, F. Barachati, A. Sridharan, S. Kéna-Cohen, *ACS Photonics* **2018**, *5*, 2921.
[36] A. Mischok, J. Lüttgens, F. Berger, S. Hillebrandt, F. Tenopala-Carmona, S. Kwon, C. Murawski, B. Siegmund, J. Zaumseil, M. C. Gather, *J. Chem. Phys.* **2020**, *153*, 20.
[37] A. Mischok, B. Siegmund, F. Le Roux, S. Hillebrandt, K. Vandewal, M. C. Gather, *Nat. Commun.* **2024**, *15*, 1.
[38] A. Mischok, S. Hillebrandt, S. Kwon, M. C. Gather, *Nat. Photonics* **2023**, *17*, 393.
[39] J. De, R. Zhao, F. Yin, C. Gu, T. Long, H. Huang, X. Cao, C. An, B. Liao, H. Fu, Q. Liao, *Light: Sci. Appl.* **2024**, *13*, 191.
[40] J. Souza, L. Benatto, G. Candiotto, L. Roman, M. Koehler, *J. Phys. Chem. A* **2022**, *126*, 1393.
[41] X. Song, N. Gasparini, L. Ye, H. Yao, J. Hou, H. Ade, D. Baran, *ACS Energy Lett.* **2018**, *3*, 669.
[42] R. Bhuyan, J. Mony, O. Kotov, G. W. Castellanos, J. Gómez Rivas, T. O. Shegai, K. Börjesson, *Chem. Rev.* **2023**, *123*, 10877.
[43] R. Saleem, A. Farhat, R. A. Khera, P. Langer, J. Iqbal, *Comput. Theor. Chem.* **2021**, *1197*, 113154.
[44] X. Zhong, S. Liu, W. You, *Sci. Adv.* **2024**, *10*, eadp8150.
[45] A. Wadsworth, M. Moser, A. Marks, M. S. Little, N. Gasparini, C. J. Brabec, D. Baran, I. McCulloch, *Chem. Soc. Rev.* **2019**, *48*, 1596.
[46] E. Moustafa, M. Méndez, J. G. Sánchez, J. Pallarès, E. Palomares, L. F. Marsal, *Adv. Energy Mater.* **2023**, *13*, 2203241.
[47] L. Zhu, M. Zhang, J. Xu, C. Li, J. Yan, G. Zhou, W. Zhong, T. Hao, J. Song, X. Xue, Z. Zhou, R. Zeng, H. Zhu, C.-C. Chen, R. C. I. MacKenzie, Y. Zou, J. Nelson, Y. Zhang, Y. Sun, F. Liu, *Nat. Mater.* **2022**, *21*, 656.
[48] H. Chen, S. Y. Jeong, J. Tian, Y. Zhang, D. R. Naphade, M. Alsufyani, W. Zhang, S. Griggs, H. Hu, S. Barlow, H. Y. Woo, S. R. Marder, T. D. Anthopoulos, I. McCulloch, Y. Lin, *Energy Environ. Sci.* **2023**, *16*, 1062.
[49] Y. Sun, L. Wang, C. Guo, J. Xiao, C. Liu, C. Chen, W. Xia, Z. Gan, J. Cheng, J. Zhou, Z. Chen, J. Zhou, D. Liu, T. Wang, W. Li, *J. Am. Chem. Soc.* **2024**, *146*, 12011.
[50] W. Yang, W. Qiu, E. Georgitzikis, E. Simoen, J. Serron, J. Lee, I. Lieberman, D. Cheyns, P. Malinowski, J. Genoe, H. Chen, P. Heremans, *ACS Appl. Mater. Interfaces* **2021**, *13*, 16766.
[51] A. B. Siddik, E. Georgitzikis, Y. Hermans, J. Kang, J. H. Kim, V. Pejovic, I. Lieberman, P. E. Malinowski, A. Kadashchuk, J. Genoe, T. Conard, D. Cheyns, P. Heremans, *ACS Appl. Mater. Interfaces* **2023**, *15*, 30534.
[52] S. Y. Park, C. Labanti, R. A. Pacalaj, T. H. Lee, Y. Dong, Y.-C. Chin, J. Luke, G. Ryu, D. Minami, S. Yun, J. Park, F. Fang, K.-B. Park, J. R. Durrant, J.-S. Kim, *Adv. Mater.* **2023**, *35*, 2306655.
[53] H. M. Luong, C. Kaiyasuan, A. Yi, S. Chae, B. M. Kim, P. Panoy, H. J. Kim, V. Promarak, Y. Miyata, H. Nakayama, T.-Q. Nguyen, *ACS Energy Lett.* **2024**, *9*, 1446.
[54] A. G. Abdelmagid, H. A. Qureshi, M. A. Papachatzakis, O. Siltanen, M. Kumar, A. Ashokan, S. Salman, K. Luoma, K. S. Daskalakis, *Nanophotonics* **2024**, *13*, 2565.
[55] X. Hu, Z. Qiao, D. Nodari, Q. He, J. Asatryan, M. Rimmele, Z. Chen, J. Martín, N. Gasparini, M. Heeney, *Adv. Opt. Mater.* **2024**, *12*, 2302210.
[56] Z. Du, H. M. Luong, S. Sabury, A. L. Jones, Z. Zhu, P. Panoy, S. Chae, A. Yi, H. J. Kim, S. Xiao, V. V. Brus, G. N. M. Reddy, J. R. Reynolds, T.-Q. Nguyen, *Adv. Mater.* **2024**, *36*, 2310478.
[57] P. Jacoutot, A. D. Scaccabarozzi, D. Nodari, J. Panidi, Z. Qiao, A. Schiza, A. D. Nega, A. Dimitrakopoulou-Strauss, V. G. Gregoriou, M. Heeney, C. L. Chochos, A. A. Bakulin, N. Gasparini, *Sci. Adv.* **2023**, *9*, eadh2694.

© 2025 The Author(s). Advanced Optical Materials published by Wiley-VCH GmbH

21951071, 0, Downloaded from https://advanced.onlinelibrary.wiley.com/doi/10.1002/adom.202501727 by Duodecim Medical Publications Ltd, Wiley Online Library on [29/08/2025]. See the Terms and Conditions (https://onlinelibrary.wiley.com/terms-and-conditions) on Wiley Online Library for rules of use; OA articles are governed by the applicable Creative Commons License